First-Year Operation of a New Water Vapor Raman Lidar at the JPL Table Mountain Facility, California

THIERRY LEBLANC, I. STUART MCDERMID, AND ROBIN A. ASPEY

Jet Propulsion Laboratory, California Institute of Technology, Wrightwood, California

(Manuscript received 23 January 2007, in final form 23 March 2007)

ABSTRACT

A new water vapor Raman lidar was recently built at the Table Mountain Facility (TMF) of the Jet Propulsion Laboratory (JPL) in California and more than a year of routine 2-h-long nighttime measurements 4–5 times per week have been completed. The lidar was designed to reach accuracies better than 5% anywhere up to 12-km altitude, and with the capability to measure water vapor mixing ratios as low as 1 to 10 ppmv near the tropopause and in the lower stratosphere. The current system is not yet fully optimized but has already shown promising results as water vapor profiles have been retrieved up to 18-km altitude. Comparisons with Vaisala RS92K radiosondes exhibit very good agreement up to at least 10 km. They also revealed a wet bias in the lidar profiles (or a dry bias in the radiosonde profiles), increasing with altitude and becoming significant near 10 km and large when approaching the tropopause. This bias cannot be explained solely by well-known too-dry measurements of the RS92K in the upper troposphere and therefore must partly originate in the lidar measurements. Excess signal due to residual fluorescence in the lidar receiver components is among the most likely candidates and is subject to ongoing investigation.

1. Introduction

Water vapor has long been identified as a key constituent of the atmosphere. Because of its particular shape, the water vapor molecule strongly absorbs infrared radiation and consequently water vapor constitutes a primary greenhouse gas. Studies have reported (e.g., de Forster and Shine 1999) that a global increase in lower-stratospheric H_2O mixing ratio, similar to that observed locally since 1981 (Oltmans and Hofmann 1995), would contribute to a surface warming reaching 40% of that responsible from CO_2 increases over the same period. The resulting lower-stratospheric cooling would be of the same order of magnitude as that caused by changes in ozone concentrations. This sensitivity of the earth's radiative balance to water vapor variations requires high-accuracy water vapor measurements (typically 3%–10%) if one wants to fully understand and properly quantify and predict future water vapor–related radiative and chemical processes that impact climate change. A large concern in this respect is that many instruments currently cannot achieve such measurement accuracy without thorough calibration and validation. The Stratospheric Processes and Their Role in Climate (SPARC) Assessment of Upper Tropospheric and Stratospheric Water Vapor (Kley et al. 2000) pointed out many discrepancies in the water vapor profiles measured by different techniques.

To contribute to the understanding of the processes involving atmospheric water vapor as well as to support the validation of satellite measurements, the Network for the Detection of Atmospheric Composition Change (NDACC, formerly known as NDSC) has recently considered including the water vapor measurements using Raman lidar in its suite of long-term measurements. A high-capability water vapor Raman lidar was therefore built at the Jet Propulsion Laboratory (JPL) Table Mountain Facility (TMF) in California (34.4°N, 117.5°W, elevation 2285 m), with the overall objective of measuring water vapor to the upper troposphere–lower stratosphere (UT/LS) with an accuracy equal to or better than 5%. The instrument went through several configurations before routine measurements were finally obtained. The present instrument configuration, leading to over a year and a half of measurements, will be described in section 2. Water vapor retrieval from Raman lidar measurements will be briefly reviewed in

Corresponding author address: Thierry Leblanc, Jet Propulsion Laboratory, California Institute of Technology, Wrightwood, CA 92397.
E-mail: leblanc@tmf.jpl.nasa.gov

DOI: 10.1175/2007JTECHA978.1

section 3. The results from 18 months of routine measurements will be presented in section 4. The last section will summarize our findings and describe our ensuing 2007 plans for instrument improvements.

2. Instrument description

Because of the very low mixing ratio of water vapor near the tropopause and in the lower stratosphere, Raman lidar measurements in this region are noise limited. To try to maximize the signal-to-noise ratio we use very high laser pulse energies of up to 900 mJ per pulse at 355 nm and a repetition rate of 10 Hz (Continuum Powerlite II Nd:YAG); a large 91-cm-aperture telescope with narrow field-of-view (fov; Intermountain Optics); and narrow 0.6-nm spectral bandwidth filters for the water vapor Raman channels (Barr Associates). The fov of the large telescope is defined by the diameter of the fiber placed at the telescope focus, which acts as the field stop. Two different fibers have been employed with core diameters of 1.0 and 1.5 mm (CeramOptec) resulting in fovs of 400 and 600 μR, respectively. For the work described in this paper, the fov of the telescope was 400 μR. A 7.5x Gallilean beam expander (CVI) is used to reduce the laser beam divergence, defined as the angle containing >95% of the laser energy, to ~300 μR. In addition to the large telescope, three 75-mm-diameter telescopes are used to collect returns from low altitudes.

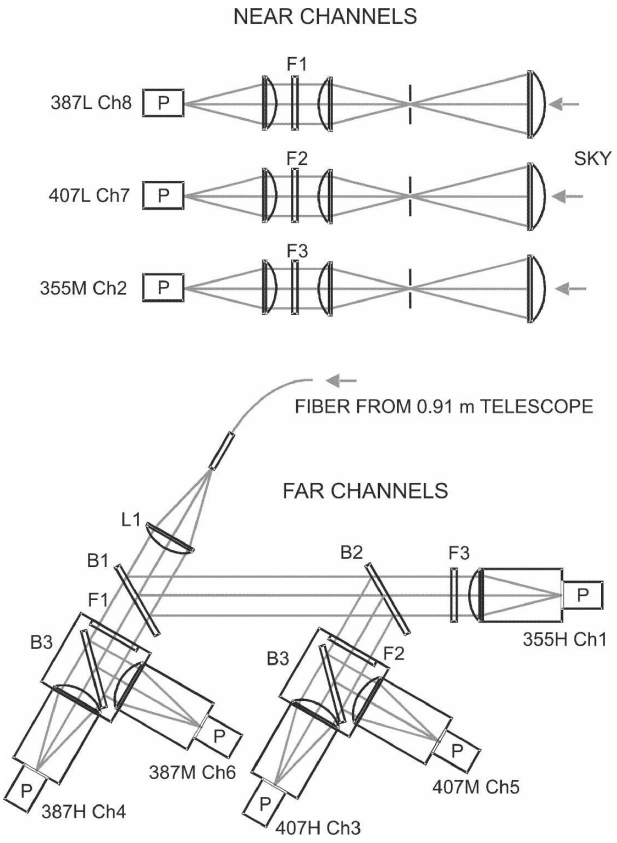

FIG. 1. TMF water vapor Raman lidar receiver between April 2005 and October 2006.

In all, the lidar receiver comprises eight channels, as shown in Fig. 1. There are three channels each for the water vapor and nitrogen Raman returns at 407 and 387 nm, respectively, and two for the elastic returns at 355 nm. The 355-nm returns are primarily used for the derivation of temperature profiles and will not be considered further in this report. Lidar returns from the large telescope are coupled to the receiver with a 4-m-long by 1.0-mm-diameter fiber. The 0.22 numerical aperture of the fiber is closely matched to the $f3$ focal ratio of the telescope for optimal coupling. The receiver employs dichroic beamsplitters (Barr Associates) at 30° incidence to separate the Raman and elastically backscattered wavelengths. Referring to Fig. 1, beamsplitter B1 transmits 387 nm at >80% while reflecting both 407 and 355 nm at >90%. The second beamsplitter, B2, reflects 407 nm at >90% and transmits 355 nm at >80%. This sequence was chosen with the assistance of Barr Associates to optimize the signal levels. Interference filters, F1–3, are used after the beamsplitters to reject out-of-band wavelengths. The 387-nm filter has a bandwidth of 1.5 nm and transmission of >75% and the 407-nm filter has a bandwidth of 0.6 nm and a transmission of ~45%. Although not shown in Fig. 1, additional E-6 355-nm blocking filters were mounted with the interference filters in the Raman channels to increase the rejection of the intense elastically scattered 355-nm radiation to ~E-12. The Raman signals from the large telescope are further divided with a ~1% beamsplitter (B3), and will be referred to as "387/407H" and "387/407M" hereafter, as indicated in Fig. 1. The signals coming through the small telescopes will be referred to as "387/407L."

The data acquisition system employs eight photon counting multichannel scalar modules (Licel TR20–160), which simultaneously acquire profiles to a maximum altitude above the site level of 124 km (16 380 bins). Each module has a bandwidth of 250 MHz with a minimum dwell time of 50 ns (7.5 m). However, 10 bins are typically summed together leading to a vertical resolution of 75 m. Data transfer uses a data acquisition (I/O) card (National Instruments PC-DIO-32HS) that interfaces the transient recorders to the acquisition PC. Miniature photomultiplier photon counting modules (Hamamatsu H5783P) are used for the detectors. A single gated Hamamatsu R7400 photomultiplier (PMT)

is used for the 355-H channel to reduce signal-induced noise (SIN) for near-field returns.

In addition to extending the dynamic range of the photon counting system, the present six-channel configuration dedicated to water vapor measurements enables better corrections for pulse pile-up saturation effects. The 387/407L channels are designed to obtain similar signal magnitude as the 387/407M channels. This then allows for the correction of overlap effects at low altitudes in signals from the large telescope.

In the early stages of instrument development, significant electromagnetic interference was picked up by a number of PMTs. The source was found to be the laser itself. To suppress the contamination several magnetic shields were placed at critical locations, one of them being between the laser and the high-intensity signals receiver box. Furthermore, shielding was placed around each PMT, all powered devices were grounded to the main table, and the Licel discriminators were increased for some of the channels, resulting only in a few sporadic episodes of contaminating noise throughout the 18-month operation.

The lidar was operated routinely from April 2005 to October 2006 in an operational mode similar to that used for the other TMF lidar systems. Measurements were performed for 2 h, 4–5 times a week, weather permitting and during the early hours of the night (typically from 2200:00 to 0000:00 LT). To optimize the beam overlap with the field-of-view of the large telescope, the 15-cm-diameter transmitter mirror is mechanically rotated on two axes until the returned signals are received optimally in the desired altitude range. This 5–10-min alignment procedure is repeated each measurement night just before the start of data acquisition. One Vaisala RS92K radiosonde (pressure–temperature–humidity only) is also launched on each measurement night, typically during the first half of the lidar experiment.

3. Water vapor retrieval

A detailed review of the Raman lidar water vapor measurement is given, for example, in Vaughan et al. (1988) and Sherlock et al. (1999a,b). The lidar signals returned in each channel are first corrected for saturation and background noise. No signal-induced noise could be detected in any of the TMF lidar channels, thus reducing the correction process to the simple extraction of a constant background noise. The signals are then range corrected, and corrected for Rayleigh extinction, ozone absorption, and overlap. After all these corrections, the signals are directly proportional to the number of Raman-backscattering molecules along the laser beam path at the measured wavelengths (i.e., nitrogen for 387 nm and water vapor for 407 nm). Assuming constant Raman cross sections at both wavelengths, the ratio of the signals at the two wavelengths is therefore proportional to the water vapor mixing ratio. When an extremely narrow filter is used (not the case here), a small correction may be necessary because of the temperature dependence of the cross sections. For the TMF lidar, the error due to statistical noise (photon counting) ranges from below 1% at 5 km to over 50% above 12 km for a 10-min integration. It is greatly reduced when averaging over 2-h or longer periods.

Unlike differential absorption lidar (DIAL) ozone and temperature lidar retrieval techniques, the water vapor Raman lidar retrieval is not self-calibrating. One calibration method consists of applying a regressive model of the unnormalized lidar water vapor profile to a profile obtained from the external measurement, for example, radiosondes. With this method the accuracy of the lidar measurements is limited by that of the instrument used for the calibration. Another calibration method is based on the use of a calibrated lamp. It has the advantage of not relying on any external measurement except that from the lamp itself. The procedure is divided into two parts. The first part is to determine the system calibration constant. The second is to measure the transmission and detection efficiency. The system calibration constant is derived from the convolution of the Raman band with the filter bandpass function along each optical path to the detector. The result is scaled by the transmission and detection efficiency measured by using a calibrated irradiance lamp applied directly to the system. The accuracy of this calibration method is dependent upon that of the calibrated lamp and to ensure its stability, the lamp needs frequent calibration sessions against National Institute of Standards and Technology (NIST) standards.

During its first year of operation, the TMF lidar was calibrated using the relative humidity measurements of Vaisala RS92K radiosondes launched simultaneously from the lidar site. Simultaneous and collocated launches are necessary conditions for a proper calibration because atmospheric water vapor is highly variable on small spatial and temporal scales. For this reason at least one radiosonde was launched for each 2-h lidar measurement period. The resulting error due to calibration is estimated to be around 3%–5%. Further details on the calibration process are given in the next section.

4. Comparisons with Vaisala RS92K radiosonde measurements

Between April 2005 and October 2006, more than 200 water vapor profiles were measured by lidar. Though data are saved every 5 or 10 min, the profiles shown here are all obtained from a standard 2-h-long measurement window. The choice of this duration reflects a compromise between a moderate laser degradation for long-term operation (i.e., favoring a lower frequency of replacement of critical parts such as flash lamps and premium optics) and sufficient signal-to-noise ratio to reach the tropopause. At least one radiosonde was launched for each 2-h-long measurement, resulting in 202 lidar-radiosonde water vapor profiles pairs. To make the lidar–radiosonde comparisons possible, relative humidity measured as a function of pressure by the radiosonde was converted into water vapor mixing ratio as a function of altitude using the classic empirical saturation vapor pressure over liquid water formulas of Hyland and Wexler (1983) and the hypsometric equation. The pressure and temperature measurements from the radiosonde are used both for the RH to mixing ratio conversion and for the derivation of geopotential height.

In Fig. 2, 4 of the 200 lidar–radiosonde water vapor profile pairs are plotted. For each profile, excellent agreement is found up to 10 km, including thin filamentary structures seen on at least three of the four profiles. The total water vapor content calculated from the radiosonde profile is reported in the bottom left corner of each plot, and points up to the high water vapor variability from one profile to another. A lidar wet bias (or radiosonde dry bias) increasing with height can be found on all but one profile. The magnitude of the bias is dependent upon the altitude of normalization. The magnitude and origin of this bias is discussed in the next section. Figures 3a–c illustrate the seasonal variations of integrated water vapor as measured by different instruments, all based at TMF. Figure 3a shows the time series between 1 April 2005 and 31 October 2006 of column water vapor integrated from the radiosonde profiles between the top of the troposphere and the altitude of 12 km. It is equivalent to a measure of upper-tropospheric water vapor. Figure 3b is identical to Fig. 3a, but for the total column (i.e., integrated between the top of the troposphere and the ground). Despite high variability, which makes the detection of any seasonal cycles difficult, the summer months seem to consistently be wetter (>20 mm) than the rest of year (<10 mm). This tendency is confirmed on Fig. 3c where the total column obtained from radiosonde, lidar, and the collocated Water Vapor Mm-Wave Spectrometer (WVMS) instrument operated by the Naval Research Laboratory (Nedoluha et al. 1995) is plotted against the day of the year. Though the microwave-retrieved total column water vapor dataset remains provisional and nonvalidated (G. E. Nedoluha 2006, personal communication), all three independent datasets reveal that July, and to a lesser extent August, are clearly the wettest months of the year, which mimics the well-known seasonal cycle of tropospheric water vapor at midlatitudes. Though most easily observed on the total water vapor content, this cycle is present throughout the troposphere on both the radiosonde and lidar partial columns (not shown here). That explains why it is well captured by lidar even though the lidar is not measuring the total column (the lidar profiles typically start 700–800 m above site). Figure 3d shows a scatterplot of water vapor total column calculated from radiosonde versus the partial column calculated from lidar (4 km to top). Despite a high degree of correlation (coefficient of 0.878), large dispersion remains, which precludes the use of integrated water vapor for an accurate calibration of the lidar at this time. However, a more sophisticated methodology will be considered in the future.

Figure 4a shows the mean radiosonde and lidar profiles of relative humidity with respect to water. The lidar mixing ratios were converted to RH using the same formulas mentioned above. Figure 4b shows the mean difference (red) together with each individual profile difference (green). As was already observable on the individual profiles of Fig. 2, there is a clear systematic wet bias on the lidar profiles (or dry bias on the radiosonde profiles), increasing from 2%–4% RH at 10 km to almost 20% RH in the lower stratosphere. The bias exceeds both instrument's 1-σ standard deviation at an altitude of 13 km (blue and purple curves on Fig. 4b). The Vaisala RS92K is the latest of a series of capacitive humidity sensors that all showed a dry bias at low humidities and cold temperatures. Historically, these dry biases were due to different problems depending on the model and type of sonde (Miloshevich et al. 2004, 2006). However, the observed dry bias between the TMF lidar and the RS92K cannot be attributed to the radiosonde dry bias alone [a correction such as that described by Miloshevich et al. (2004, 2006) would not be sufficient]. To be able to measure a few parts per million of water vapor near the tropopause, the lidar instrument is actually reaching its detection limits and is very sensitive to any contaminating signal. The most likely candidate here is residual fluorescence in the receiver. This is currently being investigated, with some details given in the concluding paragraph of this paper.

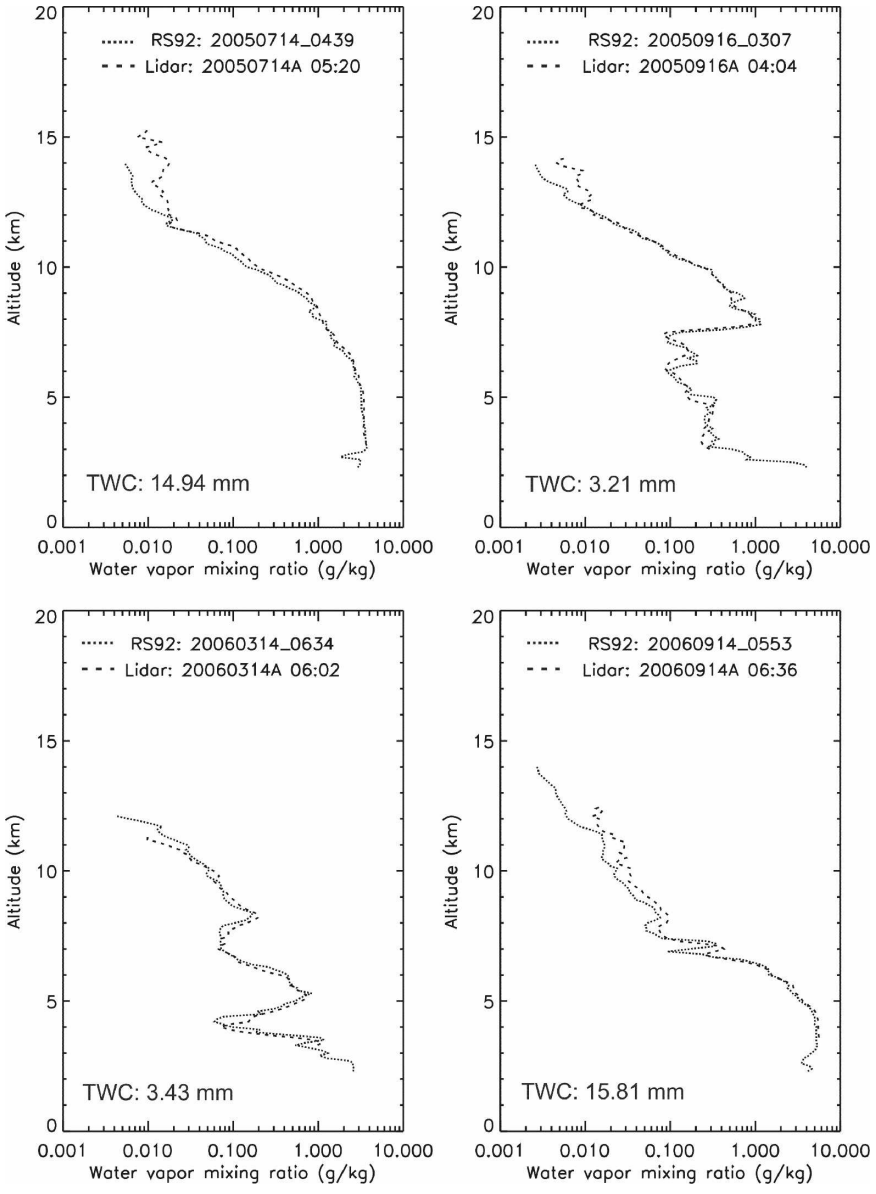

FIG. 2. Four typical simultaneous radiosonde and lidar water vapor profiles. Total water content (mm) calculated from the radiosonde profile is indicated in the lower left corner.

Not surprisingly, water vapor is seen to be highly variable from night to night. This high variability is also observed within a single night, as can be seen in Fig. 5. In this example, a layer of high relative humidity builds between 6.5 and 9 km, increasing from a low 25% at the beginning of the night to a high 90% at the end. In this figure we use 10-min integrated profiles instead of the 2-h standard window. The observed variability at short time scales is very representative of atmospheric water vapor and points out clearly the difficulty in properly calibrating the lidar using an external source of measurements. The normalization process needs to be done using measurements made as simultaneously and collocated as possible to avoid calibration errors associated with atmospheric variability. Assuming that the lidar system characteristics remain unchanged over long periods (e.g., several months), it is preferable to calculate a mean calibration constant obtained from a large number of external normalizations. This can be done by closely monitoring the lidar calibration constant over several months. Figure 6 shows the evolution over the 18 months of measurements of the TMF lidar calibration constant calculated from systematic normalizations using the

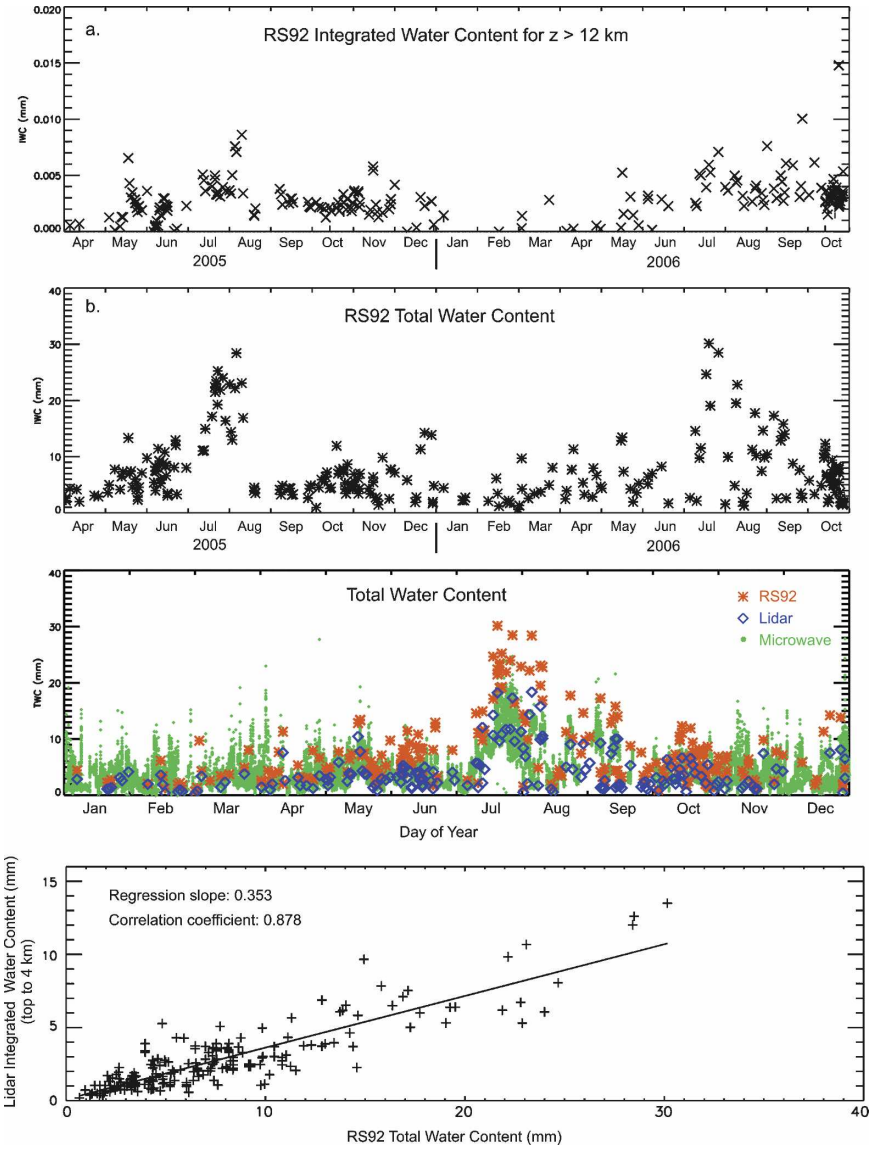

FIG. 3. Time evolution of integrated water vapor content calculated from radiosonde between (a) the tropopause and 12 km, and (b) the tropopause and the ground. (c) Total water vapor content as a function of day of year calculated from collocated radiosonde, lidar, and microwave measurements. (d) Correlation plot between RS92-measured total column and lidar-measured partial column (top to 4 km).

simultaneous radiosonde profiles. The normalization is obtained using the best fit of the nonnormalized lidar profile (387/407L signals) to the radiosonde profile in a 3–4-km-thick layer in the lower troposphere. The resulting normalization altitude is always located between 4 and 5.5 km. An average value of 0.145 and standard deviation of 0.023 (15%) were found. The standard deviation remains within both the radiosonde and lidar precisions and is well below the natural spatial and temporal variability of atmospheric water vapor. A linear fit was applied to the time series resulting in a slope of $-1.844\ 10^{-7}$ day^{-1} (i.e., -0.4% decade^{-1}), which is considerably smaller than any long-term trends expected to be detected with this lidar in the future. A few outliers were excluded from the time series before the fit was applied. The average value of 0.145 can be used for a reanalysis of the entire lidar dataset. The new profiles thus obtained are believed to be mostly absent of calibration errors related to short-scale variability.

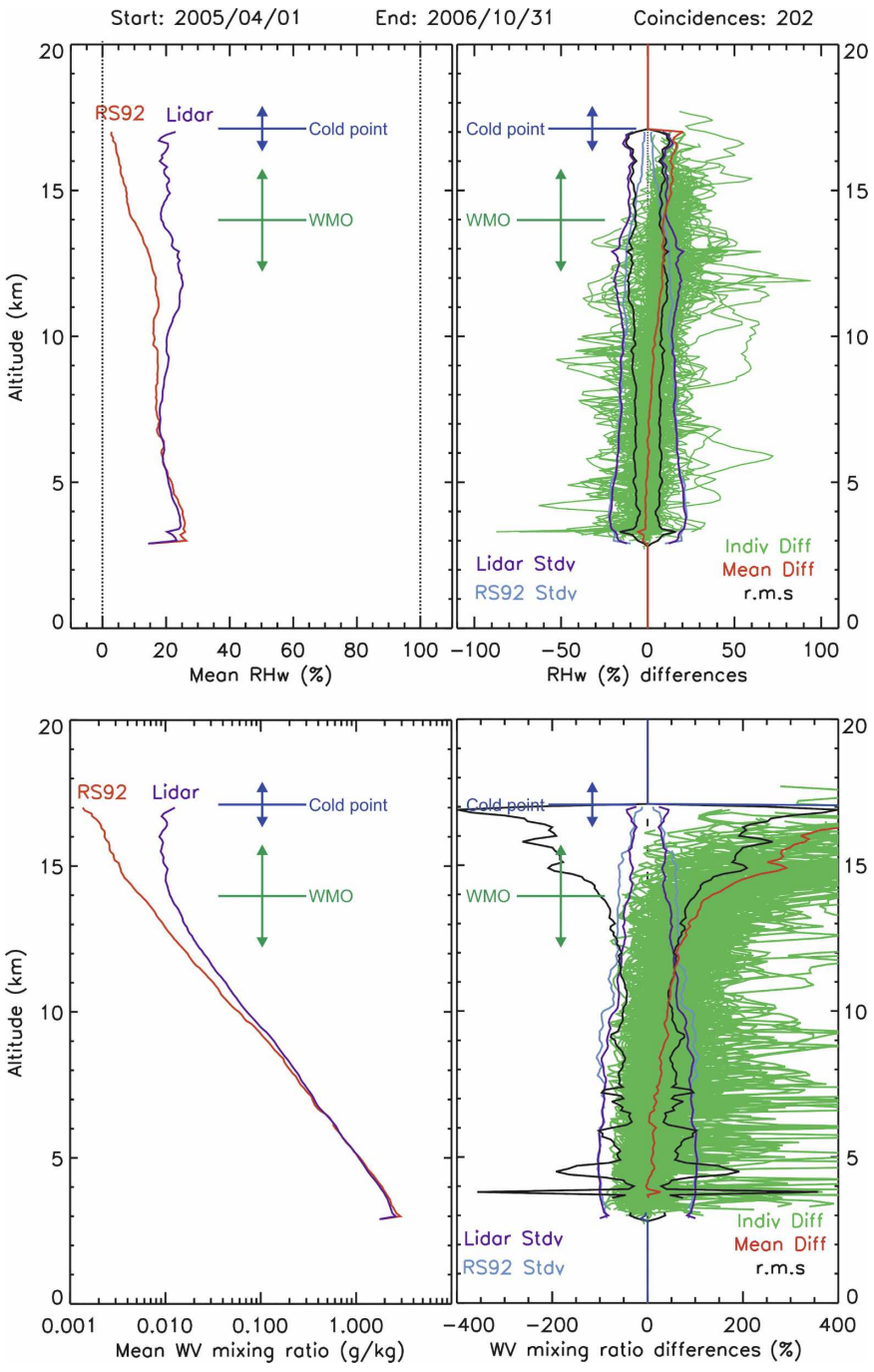

FIG. 4. (left) Mean relative humidity with respect to water, and water vapor mixing ratio profiles obtained from 202 collocated radiosonde and lidar measurements. (right) Individual (green) and mean (red) differences between the radiosonde and lidar profiles. The average heights of the tropopause [cold point and World Meteorological Organization (WMO) definitions] and their standard deviations are indicated.

5. Conclusions and perspectives

After one and a half years of routine measurements, the TMF water vapor Raman lidar has shown promising results for the long-term monitoring of upper-tropospheric water vapor. The lidar was able to measure down to 10–20 ppmv at altitudes up to 18 km. Comparisons with radiosondes showed excellent agree-

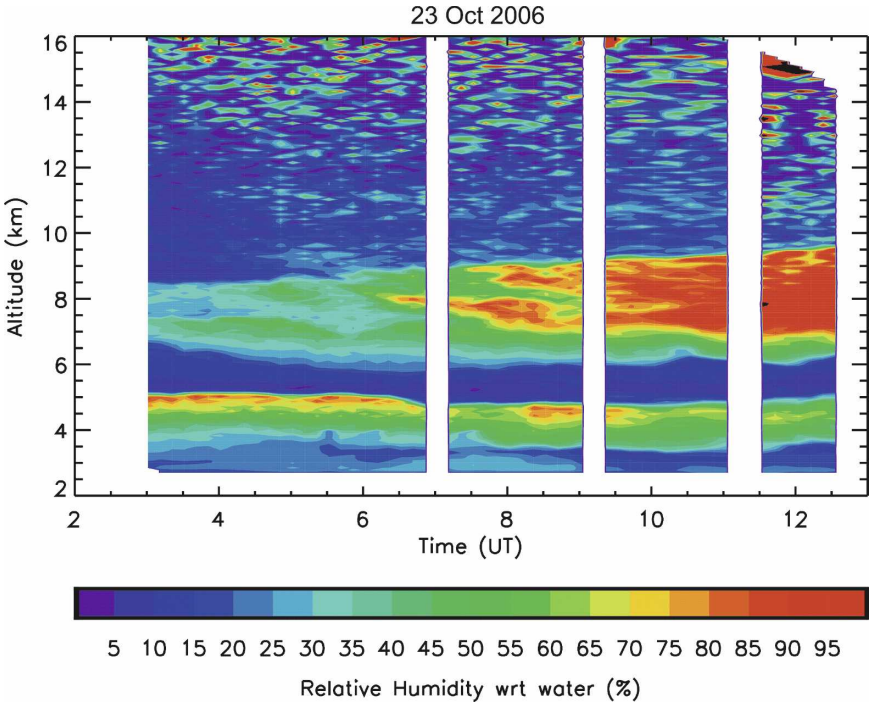

FIG. 5. Nightly evolution of relative humidity with respect to water (RHw) as measured by lidar on 23 Oct 2006.

ment for altitudes below 10 km, and a wet bias on the lidar profiles above 10–12 km. This bias increases from a few percent at 10–12 km to 100% at 16–18 km. As of today, it is difficult to properly quantify this bias as the radiosonde measurements have historically shown a well-known dry bias in very cold and dry conditions, often seen in the upper troposphere. However, because the present lidar system is pushed to its detection limits, part of the bias is thought to be due to signal contamination by residual fluorescence in the lidar receiver. This possibility is currently being investigated. Indeed the altitude dependence of the observed bias is consistent with the presence of excess signal in the water vapor channel with characteristics similar to that of Rayleigh signal-induced fluorescence. A preliminary test consisted of positioning a 355-nm blocking filter ahead of the lidar receiver fiber and comparing the resulting 407-nm signals and retrieved water vapor profiles to those obtained under the standard instrument configuration. Unlike the standard configuration, no excess signal could be observed when the blocking filter was present and the bias between lidar and radiosonde was greatly reduced. Systematic comparisons with measurements from the University of Colorado Cryogenic Frost-Point Hygrometer (CFH) (Vömel et al. 2007) are planned during the Measurements of Humidity in the

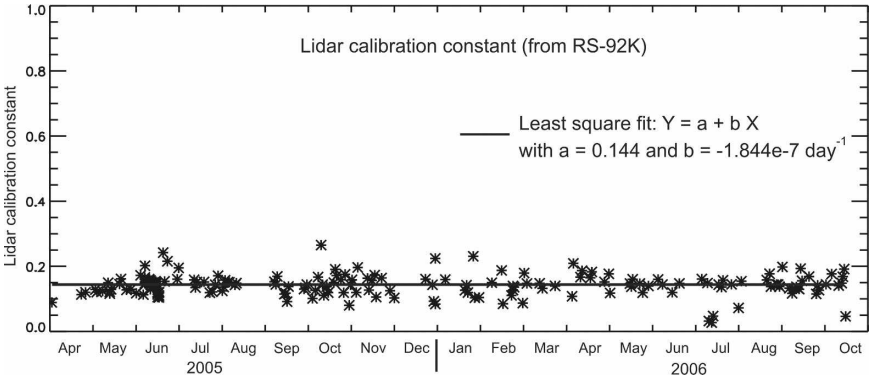

FIG. 6. Time evolution of the TMF lidar calibration constant.

Atmosphere: Validation Experiments (MOHAVE) campaign in fall 2006. Because the CFH measurements are very reliable in the UT/LS, these comparisons will help quantify the magnitude of the lidar wet bias, which in turn will help retroactively correct the lidar measurements back to April 2005. The MOHAVE campaign will involve three different lidar systems, RS92K radiosondes, the CFH, and other collocated ground-based water vapor remote sensing instruments, and should help to better characterize the TMF water vapor Raman lidar measurements throughout the troposphere.

Acknowledgments. The work described in this paper was carried out at the Jet Propulsion Laboratory, California Institute of Technology, under an agreement with the National Aeronautics and Space Administration. The authors thank Jeff Howe, who assisted in the collection of the lidar data used here. The TMF microwave integrated water content data were gratefully provided by Gerald Nedoluha from the Naval Research Laboratory.

REFERENCES

de Forster, P. M., and K. P. Shine, 1999: Stratospheric water vapor changes as a possible contributor to observed stratospheric cooling. *Geophys. Res. Lett.,* **26,** 3309–3312.

Hyland, R. W., and A. Wexler, 1983: Formulations for the thermodynamic properties of the saturated phases of H2O from 173.15K to 473.15K. *ASHRAE Trans.,* **89** (2A), 500–519.

Kley, D., J. M. Russell III, and C. Phillips, Eds., 2000: SPARC/IOC/ICSU/WCRP assessment of upper tropospheric and stratospheric water vapor. SPARC Rep. 2, 312 pp.

Miloshevich, L. M., A. Paukkunen, H. Vömel, and S. J. Oltmans, 2004: Development and validation of a time-lag correction for Vaisala radiosonde humidity measurements. *J. Atmos. Oceanic Technol.,* **21,** 1305–1327.

——, H. Voemel, D. N. Whiteman, B. M. Lesht, F. J. Schmidlin, and F. Russo, 2006: Absolute accuracy of water vapor measurements from six operational radiosonde types launched during AWEX-G, and implications for AIRS validation. *J. Geophys. Res.,* **111,** D09S10, doi:10.1029/2005JD006083.

Nedoluha, G. E., R. M. Bevilacqua, R. M. Gomez, D. L. Thacker, W. B. Waltman, and T. A. Pauls, 1995: Ground-based measurements of water vapor in the middle atmosphere. *J. Geophys. Res.,* **100,** 2927–2939.

Oltmans, S. J., and D. J. Hofmann, 1995: Increase in lower stratospheric water vapor at a midlatitude Northern Hemisphere site from 1981 to 1994. *Nature,* **374,** 146–149.

Sherlock, V., A. Garnier, A. Hauchecorne, and P. Keckhut, 1999a: Methodology for the independent calibration of Raman backscatter water vapor lidar systems. *Appl. Opt.,* **38,** 5816–5837.

——, ——, ——, and ——, 1999b: Implementation and validation of a Raman lidar measurement of middle and upper tropospheric water vapor. *Appl. Opt.,* **38,** 5838–5850.

Vaughan, G., D. P. Waring, L. Thomas, and V. Mitev, 1988: Humidity measurements in the free troposphere using Raman backscatter. *Quart. J. Roy. Meteor. Soc.,* **114,** 1471–1484.

Vömel, H., D. David, and K. Smith, 2007: Accuracy of tropospheric and stratospheric water vapor measurements by the Cryogenic Frost point Hygrometer (CFH): Instrumental details and observations. *J. Geophys. Res.,* **112,** D08305, doi:10.1029/2006JD007224.